Mitochondrial E3 ubiquitin ligase MARCH5 controls mitochondrial fission and cell sensitivity to stress-induced apoptosis through regulation of MiD49 protein

Shan Xu[a,b,*], Edward Cherok[a,b,*], Shweta Das[a,b], Sunan Li[a,b], Brian A. Roelofs[a,b,c], Shealinna X. Ge[c], Brian M. Polster[c], Liron Boyman[a,d], W. Jonathan Lederer[a,d], Chunxin Wang[e], and Mariusz Karbowski[a,b]

[a]Center for Biomedical Engineering and Technology, [b]Department of Biochemistry and Molecular Biology, [c]Department of Anesthesiology and the Shock, Trauma and Anesthesiology Research (STAR) Center, and [d]Department of Physiology, University of Maryland School of Medicine, Baltimore, MD 21201; [e]Biochemistry Section, Surgical Neurology Branch, National Institute of Neurological Disorders and Stroke, National Institutes of Health, Bethesda, MD 20892

ABSTRACT Ubiquitin- and proteasome-dependent outer mitochondrial membrane (OMM)-associated degradation (OMMAD) is critical for mitochondrial and cellular homeostasis. However, the scope and molecular mechanisms of the OMMAD pathways are still not well understood. We report that the OMM-associated E3 ubiquitin ligase MARCH5 controls dynamin-related protein 1 (Drp1)-dependent mitochondrial fission and cell sensitivity to stress-induced apoptosis. MARCH5 knockout selectively inhibited ubiquitination and proteasomal degradation of MiD49, a mitochondrial receptor of Drp1, and consequently led to mitochondrial fragmentation. Mitochondrial fragmentation in MARCH5^{−/−} cells was not associated with inhibition of mitochondrial fusion or bioenergetic defects, supporting the possibility that MARCH5 is a negative regulator of mitochondrial fission. Both MARCH5 re-expression and MiD49 knockout in MARCH5^{−/−} cells reversed mitochondrial fragmentation and reduced sensitivity to stress-induced apoptosis. These findings and data showing MARCH5-dependent degradation of MiD49 upon stress support the possibility that MARCH5 regulation of MiD49 is a novel mechanism controlling mitochondrial fission and, consequently, the cellular response to stress.

INTRODUCTION

The outer mitochondrial membrane (OMM) plays a critical role in various mitochondrial functions, including the regulation of apoptosis (Youle and Strasser, 2008), autophagy (Hailey et al., 2010; Germain et al., 2011), and mitochondrial membrane fusion and fission (Youle and van der Bliek, 2012; Mishra and Chan, 2014). Consistent with this, stringent control of the abundance and activity of OMM-associated proteins is vital for maintaining mitochondrial and cellular function.

In eukaryotes, short-lived proteins are degraded by the ubiquitin (Ub)/proteasome system (UPS). In addition to other substrates, UPS also controls the degradation of OMM-associated proteins. Several E3 Ub ligases associated with or acting on the mitochondria have been identified, including MARCH5/MITOL (Nakamura et al., 2006; Yonashiro et al., 2006; Karbowski et al., 2007), IBRDC2 (Benard et al., 2010), Parkin (Narendra et al., 2008), ARF-BP1/Mule (Zhong et al., 2005), SCF[FBW7] (Inuzuka et al., 2011), and the deubiquitinases Usp30 (Nakamura and Hirose, 2008) and Usp9x
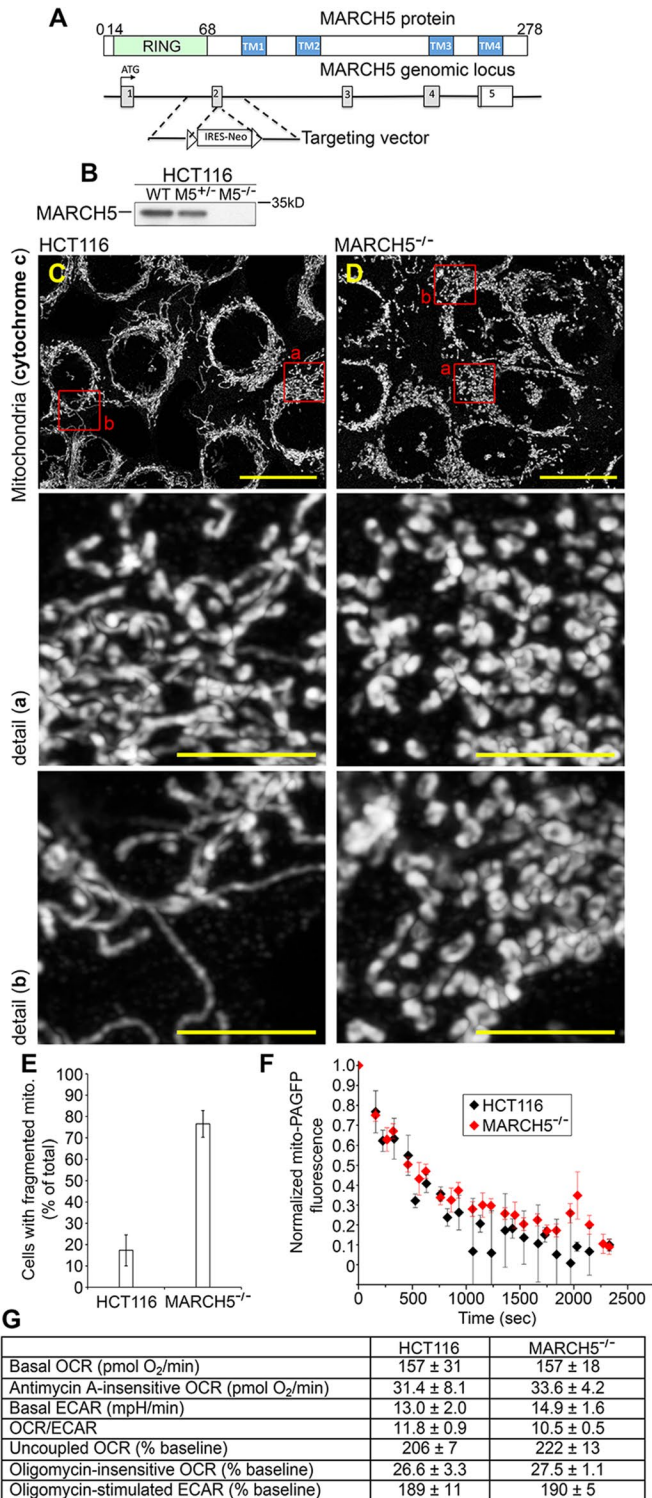
FIGURE 1: Mitochondria in MARCH5$^{-/-}$ cells. (A) Schematic of MARCH5 protein and MARCH5$^{-/-}$ cell generation. (B) Western blot analysis of MARCH5 in wild-type, MARCH5$^{+/-}$, and MARCH5$^{-/-}$ HCT116 cells. (C and D) Wild-type (C) and MARCH5$^{-/-}$ (D) HCT116 cells were immunostained for cytochrome *c* to detect mitochondria; this was followed by Airyscan superresolution imaging. Scale bars: 20 μm and 5 μm (detail images). Maximum intensity projections are shown. (E) Mitochondrial morphology was quantified in wild-type and MARCH5$^{-/-}$ HCT116 cells. Data represent mean ± SD of five independent counts of 150 cells/condition. (F) Mitochondrial fusion rates in wild-type and MARCH5$^{-/-}$ cells. mito-PAGFP fluorescence

(Schwickart *et al.*, 2010). Collectively these proteins control critical mitochondria-associated homoeostatic events, including stress response, mitochondrial membrane dynamics, and mitochondrial steps in apoptosis.

The OMM-associated E3 Ub ligase MARCH5 was initially proposed to control mitochondrial fusion and/or fission. It was reported that MARCH5 interacts with Mfn1, Mfn2, and dynamin-related protein 1 (Drp1) and controls these proteins through a Ub-dependent but largely unspecified mechanism (Nakamura *et al.*, 2006; Yonashiro *et al.*, 2006; Karbowski *et al.*, 2007). Since the initial discovery, several reports have suggested that various targets and pathways may be regulated by MARCH5, including mitochondria–endoplasmic reticulum interactions (Sugiura *et al.*, 2013), cellular senescence (Park *et al.*, 2010), and removal of disease-causing misfolded proteins from the mitochondria (Yonashiro *et al.*, 2009; Sugiura *et al.*, 2011). This relatively broad spectrum of MARCH5-controlled pathways suggests a critical role for MARCH5 in the maintenance of mitochondrial homeostasis. Even with these insights, the scope and molecular mechanisms of how MARCH5 monitors and influences mitochondria are still not well understood.

In this paper, we show that MARCH5 is essential for regulation of MiD49, an OMM-associated receptor of mitochondrial fission factor Drp1 (Palmer *et al.*, 2011, 2013; Loson *et al.*, 2013). Our data also showed that MARCH5 controls degradation of MiD49 upon stress. Consistent with this, MARCH5-deficient cells displayed increased sensitivity to stress-induced apoptosis. These findings highlight the critical role of MARCH5 in the coordination of mitochondrial fission rates with OMM-related mitochondrial stress responses.

RESULTS AND DISCUSSION
Role of MARCH5 in mitochondrial membrane dynamics and bioenergetics

Using homologous recombination gene-targeting technology, we generated a biallelic MARCH5 knockout in human colorectal carcinoma HCT116 cells (MARCH5$^{-/-}$; Figure 1, A and B). Motivated by reports suggesting that MARCH5 plays a role in mitochondrial fusion or fission (Nakamura *et al.*, 2006; Yonashiro *et al.*, 2006; Karbowski *et al.*, 2007), we sought to investigate the possible effect of MARCH5 depletion on mitochondrial network organization. To this end, cells were immunostained for cytochrome *c*, a marker of mitochondrial intermembrane space (Figure 1, C and D); this was followed by Airyscan superresolution imaging. Consistent with RNA interference (RNAi) studies (Nakamura *et al.*, 2006; Yonashiro *et al.*, 2006), MARCH5 knockout led to increases in the number of cells showing mitochondrial fragmentation (Figure 1, D and E), as compared with wild-type cells (Figure 1, C and E). While MARCH5 was suggested to regulate both mitochondrial fusion and fission (Nakamura *et al.*, 2006; Yonashiro *et al.*, 2006; Karbowski *et al.*, 2007; Fang *et al.*, 2013), the effect of MARCH5 depletion on mitochondrial fusion rates has not been reported. To determine mitochondrial fusion rates, we applied a mitochondrial matrix–targeted photoactivatable green fluorescent protein (mito-PAGFP)-based mitochondrial fusion assay (Karbowski *et al.*, 2004). Quantification of

changes were quantified and plotted as a function of time as shown in the figure. Initial postactivation values were normalized to 1. Data represent mean ± SEM of 51 (wild-type) and 43 (MARCH5$^{-/-}$) single-cell time-lapse experiments. (G) Bioenergetic properties of wild-type and MARCH5$^{-/-}$ HCT116 cells are shown. Data represent mean ± SE from five to seven independent experiments/group. None of the differences is significant ($p > 0.05$).

mito-PAGFP in several time-lapse experiments revealed similar mito-PAGFP fluorescence dilution rates in wild-type cells and MARCH5$^{-/-}$ cells, consistent with unaltered mitochondrial fusion dynamics (Figure 1F).

It has also been reported that inhibition of mitochondrial fusion in Mfn1-, Mfn2-, and Opa1-depleted cells resulted in aberrant bioenergetic performance of the mitochondria. Bioenergetic dysfunctions can also induce mitochondrial fragmentation, mostly through abnormal processing of Opa1 and consequent inhibition of mitochondrial fusion (for a review, see Karbowski, 2010; Chan, 2012). We analyzed the effect of MARCH5 depletion on cellular bioenergetics by measuring cellular oxygen consumption rate (OCR) and extracellular acidification rate (ECAR). The data showed that MARCH5$^{-/-}$ cells did not differ from wild-type cells in basal OCR, antimycin A (AntA)-insensitive nonmitochondrial OCR, basal ECAR, OCR/ECAR ratio, uncoupled OCR, oligomycin-insensitive OCR, or oligomycin-stimulated ECAR (Figure 1G). Therefore, given the unaltered mitochondrial fusion and bioenergetics in MARCH5$^{-/-}$ cells, as compared with wild-type cells, the mitochondrial fragmentation observed in MARCH5$^{-/-}$ cells may be due to increased mitochondrial fission. Under this scenario, MARCH5 activity would be required for hindering mitochondrial fission rates.

Identification of MARCH5-controlled proteins

Taking advantage of MARCH5 deficiency in MARCH5$^{-/-}$ cells (Figures 1B and Supplemental Figure S1A), we analyzed the levels of an array of proteins with a focus on those associated with the OMM (Supplemental Figure S1, A and B). If MARCH5 controls turnover of certain proteins, then these proteins would be more abundant in MARCH5-depleted cells, as compared with parental HCT116 cells. Total-cell lysates obtained from wild-type and MARCH5$^{-/-}$ cells were subjected to Western blot analysis (Supplemental Figure S1A) followed by densitometric quantification of respective proteins from several independent experiments (Supplemental Figure S1B). The data showed relatively unaltered levels of most of the analyzed proteins (Supplemental Figure S1). Two exceptions were major increases in levels of Mcl1, an antiapoptotic Bcl2 family protein (9.3 ± 0.8–fold increase over Mcl1 levels in wild-type cells; Supplemental Figure S1A), and MiD49, an OMM protein proposed to participate in mitochondrial fission and perhaps fusion (Palmer et al., 2011; Liu et al., 2013; 5.7 ± 0.7–fold increase over MiD49 levels in wild-type cells; Supplemental Figure S1, A and B). Because other analyzed OMM-associated Bcl2 family and mitochondrial fusion/fission proteins, including MiD49 homologue MiD51, were not changed or were altered to a much lesser degree (Supplemental Figure S1), these data suggested a specific role for MARCH5 in regulation of MiD49 and Mcl1 protein levels. However, because we found that ubiquitination of Mcl1 does not require MARCH5 activity (unpublished data), these data suggest that observed changes in Mcl1 might be indirect, and further studies were therefore focused on MiD49.

To verify the specificity of MARCH5 depletion on MiD49 levels, we applied short hairpin RNA (shRNA) to down-regulate MARCH5 in HeLa cells (Figure 2A). Consistent with MARCH5$^{-/-}$ cells, MiD49 accumulation upon MARCH5 down-regulation was detected with five independent shRNA constructs (Figure 2A). We also down-regulated p97, an AAA-ATPase required for retrotranslocation of OMM-associated proteins before their proteasomal degradation (Xu et al., 2011). The data showed an increase in MiD49 in p97 RNAi cells obtained using two verified p97 shRNA constructs (Xu et al., 2011; Figure 2A), confirming MiD49 as a substrate of OMM-associated degradation. Consistent with this notion, subcellular fractionation revealed mitochondrial accumulation of MiD49 in MARCH5$^{-/-}$ cells (Figure 2B).

We then tested the effects of MARCH5 re-expression on MiD49 levels in MARCH5$^{-/-}$ cells. Cells were transfected with MYC-tagged MARCH5 (MYC-MARCH5); this was followed by Western blot analysis. The data showed a prominent decrease of MiD49 in MYC-MARCH5-expressing MARCH5$^{-/-}$ cells (Figure 2C), confirming a specific role for MARCH5 in the control of MiD49 levels.

MARCH5 controls MiD49 ubiquitination and turnover

To determine the degree to which MARCH5 controls MiD49 turnover rates, we treated wild-type and MARCH5$^{-/-}$ cells with protein synthesis inhibitor cycloheximide (CHX); this was followed by Western blot analysis (Figure 2D). Densitometric evaluations of the Western blot data revealed an ~2-h half-life of MiD49 in wild-type cells (Figure 2E), indicating the relatively unstable nature of this protein. On the other hand, inhibition of MiD49 degradation was observed in CHX-treated MARCH5$^{-/-}$ cells (Figure 2, D and E), which further validated the notion that MARCH5 controls the turnover of MiD49. Of note, it appears that MiD49 has the second-shortest half-life after Mcl1 among endogenous OMM-associated proteins (both reported and from our analysis; Figure 2E and unpublished data). In comparison, the half-life of the OMM-associated protein Mff (mitochondrial fission factor) (Gandre-Babbe and van der Bliek, 2008) was estimated to be more than 8 h (Figure 2, D and F).

These results suggested that MARCH5 might function as a MiD49-ubiquitinating E3 Ub ligase that regulates proteasomal degradation of this protein. For testing this possibility, MiD49 was immunoprecipitated from denatured wild-type and MARCH5$^{-/-}$ cell lysates. To stabilize MiD49 ubiquitination, we treated cells for 8 h with the proteasome inhibitor MG132. Our attempts to immunoprecipitate sufficient amounts of endogenous MiD49 using commercially available antibodies were unsuccessful (unpublished data). Therefore, for MiD49 immunoprecipitation, wild-type and MARCH5$^{-/-}$ cells were transfected with MYC-tagged MiD49 (MYC-MiD49) followed by treatments described above. Untransfected cells were used as a control (Figure 2, G and H). Higher levels of Ub were detected in MYC-MiD49 immunoprecipitates from HCT116 cells, as compared with MARCH5$^{-/-}$ cells and control untransfected cells (Figure 2, G and H, red rectangle in H). Consistent with the role of MARCH5-mediated ubiquitination in proteasomal degradation of MiD49, a substantial increase of poly-Ub in MYC-MiD49 immunoprecipitates was detected in MG132-treated wild-type but not in MG132-treated MARCH5$^{-/-}$ cells and MG132-treated untransfected cells (Figure 2, G and H). Thus our findings reveal that ubiquitination of MiD49 depends on MARCH5. This conclusion was further verified by data showing rescue of MG132-stabilized MiD49 ubiquitination in samples immunoprecipitated from MARCH5$^{-/-}$ cells cotransfected with MYC-MiD49 and YFP-tagged wild-type MARCH5 (YFP-MARCH5; Figure 2I). Supporting the importance of MARCH5 RING-domain activity for MiD49 ubiquitination, YFP-tagged RING domain activity–deficient MARCH5 mutant (YFP-MARCH5^{H43W}; Yonashiro et al., 2006; Karbowski et al., 2007) had a less pronounced effect (Figure 2I).

MARCH5 controls the mitochondrial network through an MiD49-dependent mechanism

We tested the role of MiD49 in mitochondrial fragmentation observed in MARCH5$^{-/-}$ cells (Figure 1, D and E). CRISPR/Cas9-mediated genome editing was used to knock out MiD49 in wild-type (MiD49$^{-/-}$) and MARCH5$^{-/-}$ HCT116 cells (DKO). MiD49 knockout was confirmed by PCR (unpublished data) and Western blot (Figure 3G). Considering the reported role for MiD49 in the control of the cellular distribution of Drp1 (Palmer et al., 2011), cells were immunostained for Drp1 together with Tom20, a marker of the
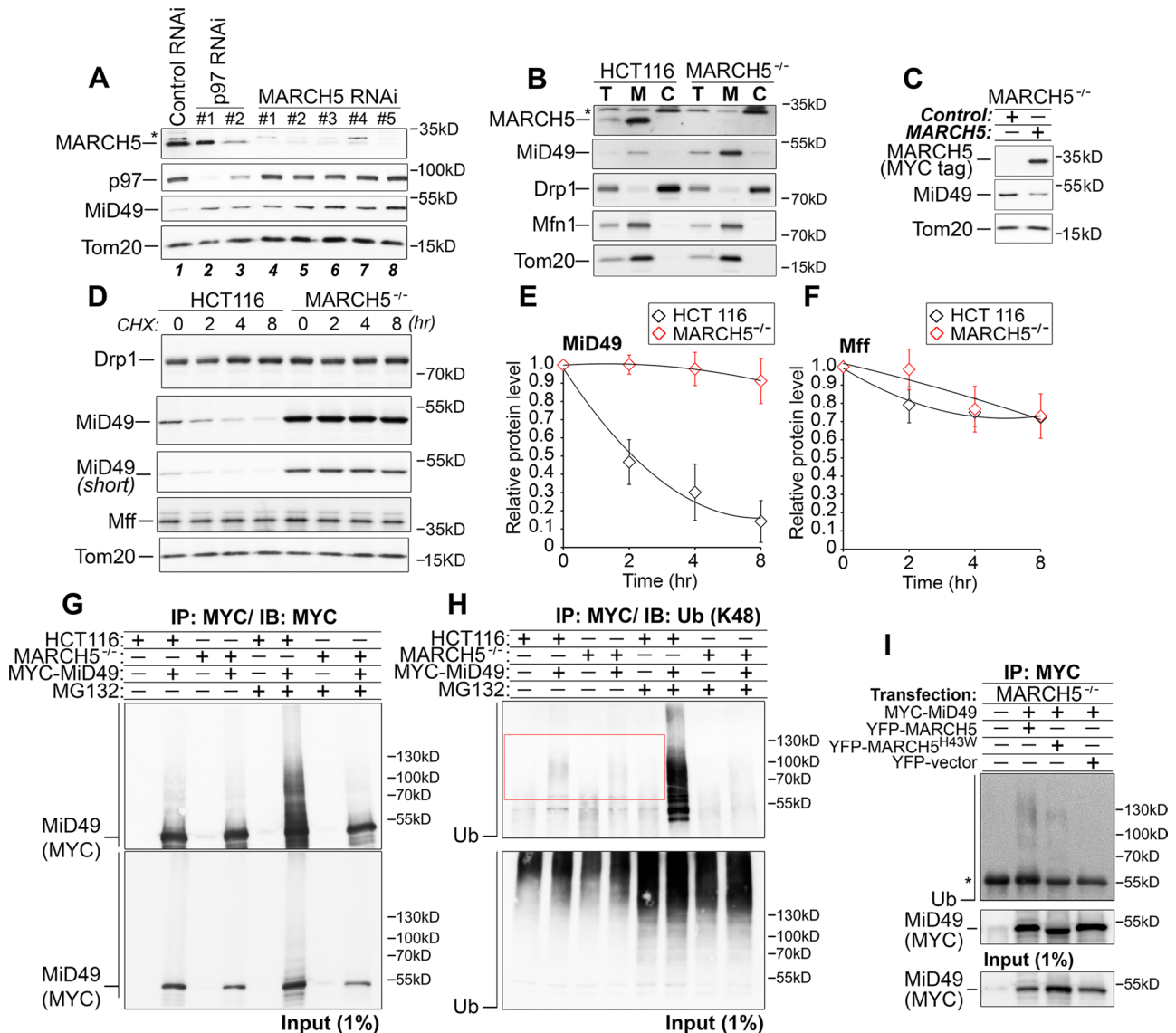
FIGURE 2: MARCH5 controls ubiquitination and proteasomal degradation of MiD49. (A) Total cell lysates obtained from HeLa cells transfected with five different MARCH5 shRNA constructs (1–5; lanes 4–8), two different p97 shRNA constructs (lanes 2 and 3), or a GFP shRNA construct (Control; lane 1) were analyzed by Western blot as indicated. (B) Wild-type and MARCH5$^{-/-}$ cells were subjected to cell fractionation to obtain total-cell lysates (T), mitochondria-enriched heavy membrane fractions (M), and postmitochondrial cytosolic fractions (C), followed by Western blot as indicated. *, an x-reactive band detectable with anti-MARCH5 antibody. (C) Western blot analysis of vector (Control)- and MYC-MARCH5 (*MARCH5*)-transfected MARCH5$^{-/-}$ cells. Cells were analyzed for the levels of MiD49 and MYC-MARCH5. Tom20 was used as a loading control. (D) Wild-type and MARCH$^{-/-}$ cells were treated with CHX as indicated, followed by Western blot to detect MiD49 (two exposures of the same MiD49 blot are shown), Drp1 and Mff. Tom20 served as a loading control. (E and F) Relative MiD49 (E) and Mff (F) protein levels in wild-type and MARCH$^{-/-}$ cells were quantified and plotted as a function of time of CHX treatment. Protein levels detected in untreated samples (0 min) were set at 1. (G and H) Control or MG132-treated (8 h) wild-type and MARCH5$^{-/-}$ cells transfected with MYC-MID49 were subjected to MYC immunoprecipitation under denatured conditions. Samples were analyzed by Western blot for MYC-tag (to detect MYC-MiD49; G) and Ub (H) as indicated (top panels in G and H). Inputs (1% of lysates used for immunoprecipitation) are shown in the bottom panels in G and H. (I) MARCH5$^{-/-}$ cells transfected with MYC-MiD49 alone, cotransfected with MYC-MiD49 and YFP-MARCH5 or MYC-MiD49 and YFP-MARCH5^{H43W}, or MYC-MiD49 and YFP-vector were treated with MG132 for 8 h, followed by MYC immunoprecipitation under denatured conditions and then Western blot as indicated. *, antibody heavy chain.

OMM; this was followed by Airyscan superresolution imaging (Figure 3, A–F). The data showed complete reversal of mitochondrial fragmentation in DKO cells (Figure 3, F and H). While ~70% of MARCH5$^{-/-}$ cells displayed a fragmented mitochondrial network (Figure 3, B and H), fragmented mitochondria were detected in only ~1% of DKO cells (Figure 3, F and H). Because similar results were observed in two DKO clones generated with CRISPR targeting MID49 exon2 and two DKO clones generated with CRSPR
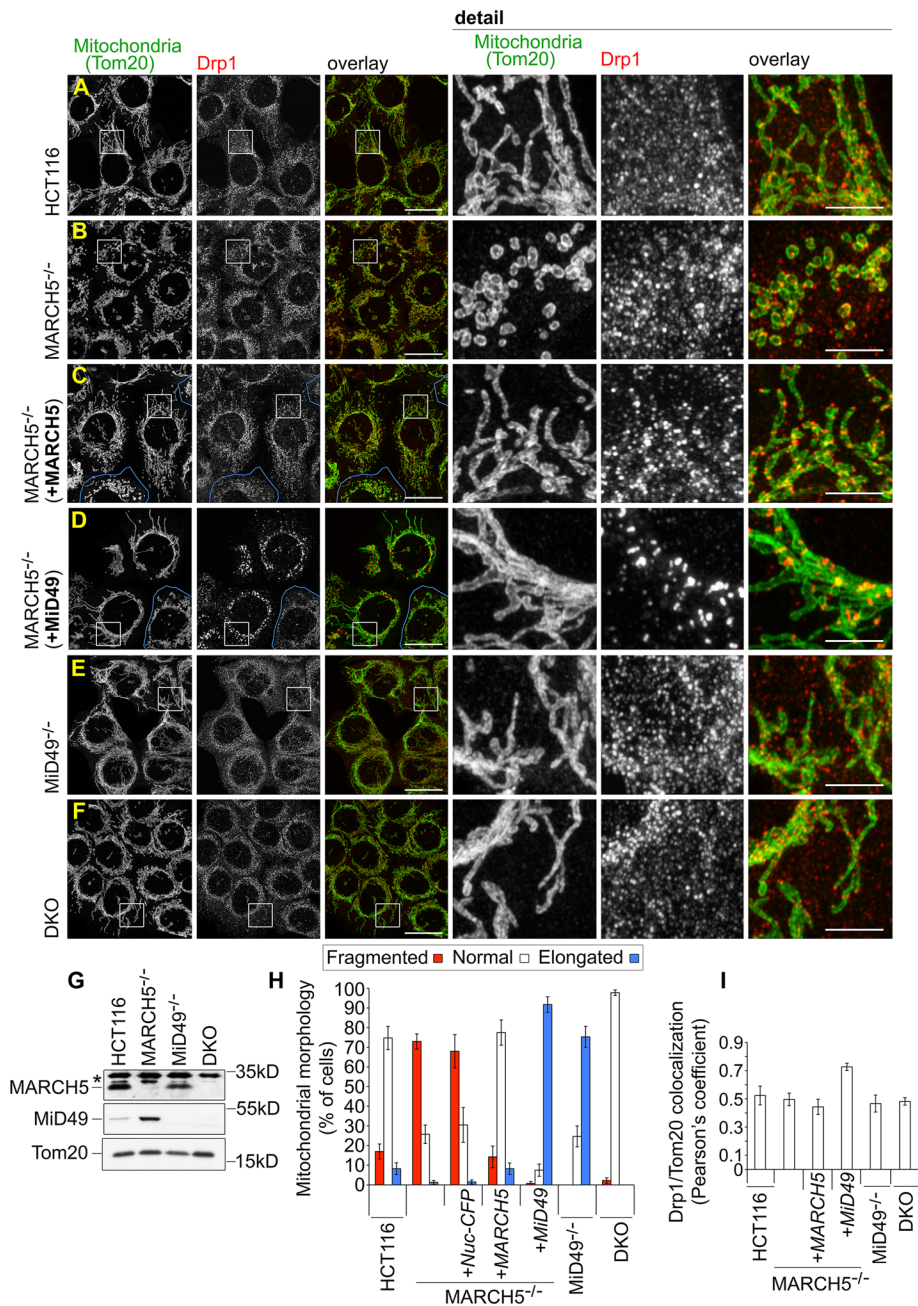
FIGURE 3: Mitochondrial network organization. (A–E) Typical examples of mitochondrial morphology (Tom20; green on overlay images) and Drp1 (red on overlay images) in wild-type (A), MARCH5$^{-/-}$ (B–D), MiD49$^{-/-}$ (E), and MARCH5$^{-/-}$/MiD49$^{-/-}$ (DKO; F) cells are shown. In C, MARCH5$^{-/-}$ cells were cotransfected with MYC-MARCH5 and nucleus-targeted cyan fluorescent protein (Nuc-CFP; unpublished data) to identify transfected cells. In D MARCH5$^{-/-}$ cells were cotransfected with MYC-MiD49 and Nuc-CFP, as above. Nontransfected cells are overlaid with blue lines. Scale bars: 20 μm and 5 μm (detail images). (G) MARCH5 and MiD49 protein levels in wild-type, MARCH5$^{-/-}$, MiD49$^{-/-}$, and MARCH5$^{-/-}$/MiD49$^{-/-}$ (DKO) cells. Tom20 was used as a loading control. (H) Mitochondrial morphology was quantified in cells indicated in the figure. Data represent the mean ± SD of three independent counts of 150 cells/condition. (I) Colocalization of Drp1 with mitochondria was analyzed. The values represent Pearson's correlation coefficients. Data represent the mean ± SD of 30–50 cells/condition.

targeting MID49 exon4 (unpublished data), the effect of MiD49 knockout on mitochondrial morphology appears to be specific. Furthermore, re-expression of MARCH5 in MARCH5$^{-/-}$ cells reduced MiD49 protein levels (Figure 2C) and rescued mitochondrial fragmentation, leading to formation of normal tubular mitochon-

dria (Figure 3, C and H). Thus mitochondrial fragmentation in MARCH5$^{-/-}$ cells was likely the result of abnormal MiD49 accumulation. However, as reported earlier (Palmer et al., 2011), further MiD49 overexpression induced mitochondrial elongation/interconnection in ~100% of wild-type (unpublished data) and MARCH5$^{-/-}$ (Figure 3, D and H) cells. Thus it is possible that, while high levels of MiD49 could interfere with mitochondrial fission, less pronounced MiD49 increases could accelerate mitochondrial fission leading to mitochondrial fragmentation. Indeed, in MiD49$^{-/-}$ cells, low levels of ectopic MYC-MiD49 induced mitochondrial fragmentation, while mitochondrial elongation was apparent in cells expressing high levels of MYC-MiD49 (unpublished data).

We did not detect marked differences in Drp1 localization in analyzed cells (Figures 2B and 3, A–F and I), suggesting that either mitochondrial accumulation of Drp1 is not detectably affected by changes in MiD49 expression or that other Drp1 receptors compensate for MiD49 depletion. While it has been shown that Drp1 accumulated on mitochondria in MiD49- and MiD51-overexpressing cells (Palmer et al., 2011), an approximately sixfold increase of MiD49 protein in MARCH5$^{-/-}$ cells, as shown here (Supplemental Figure S1), may not be sufficient to affect Drp1 recruitment to the mitochondria. However, further MiD49 overexpression induced abnormal mitochondrial assembly of Drp1 in MARCH5$^{-/-}$ cells (Figure 3, D and I).

Role of MARCH5 in stress-induced degradation of MiD49

Considering the relatively unstable nature of MiD49 (Figure 2, D and E), which suggests a signaling role for this protein, we sought to determine whether MARCH5 controls MiD49 stability under stress (Figure 4). Wild-type and MARCH5$^{-/-}$ cells were treated with two unrelated inducers of mitochondria-dependent apoptosis, actinomycin D (ActD; Figure 4, A–D) and staurosporine (STS; Figure 4, E–H) for 0, 2, 4, and 8 h and were analyzed by Western blot as indicated in Figure 4, A–H. While treatments with ActD and STS led to a gradual reduction of MiD49 protein levels in wild-type cells, degradation of MiD49 was not detectable in MARCH5$^{-/-}$ cells (Figure 4, A, D, E, and H). Thus MARCH5 appears to control apoptosis-induced MiD49 degradation. Notably, the proteasome inhibitor MG132 hindered ActD- and STS-induced MiD49 degradation in a manner similar to degradation of Mcl1, an established proteasome substrate (Figure 4, I and J), indicating that MARCH5- and proteasome-dependent degradation of MiD49
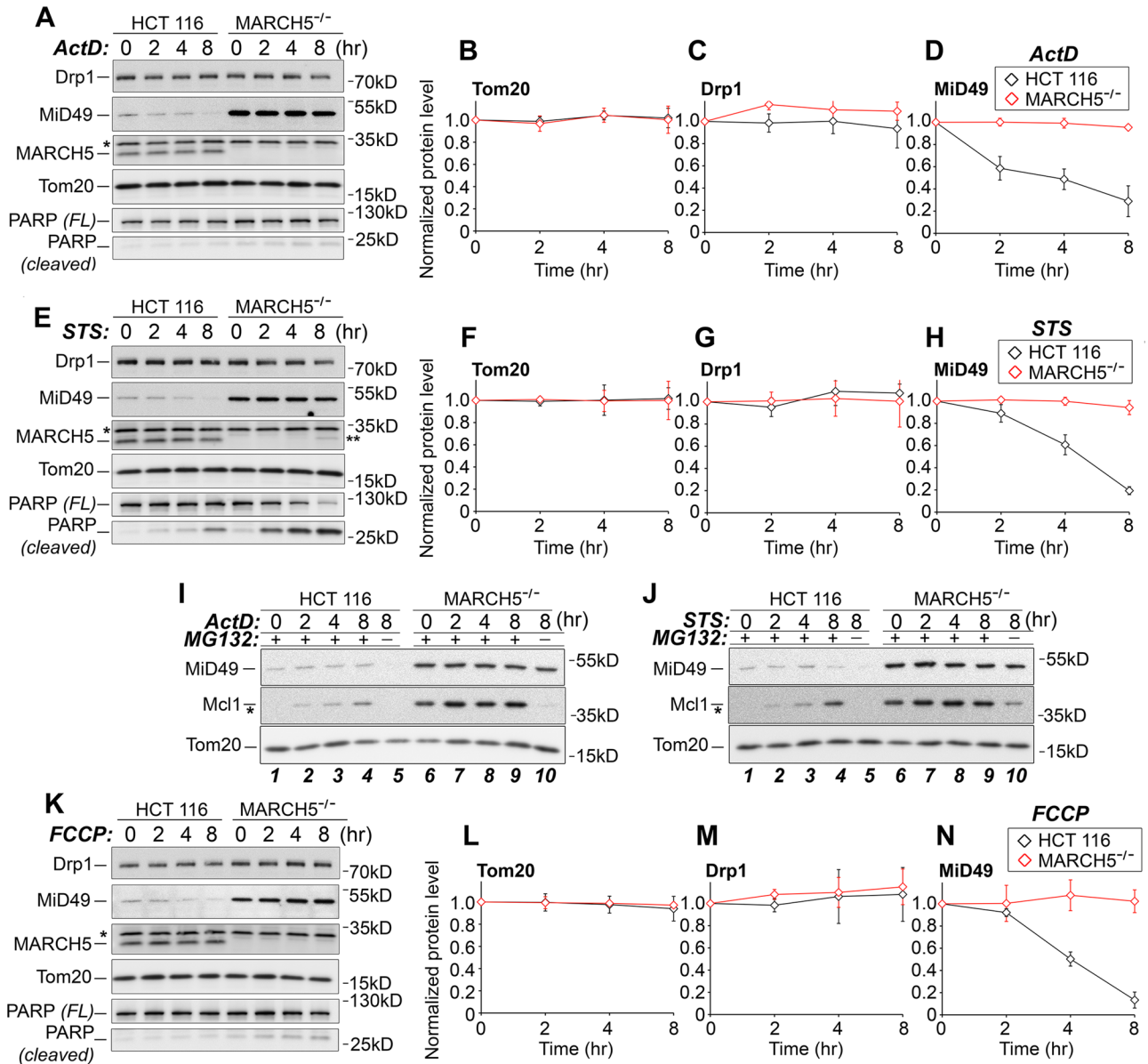
FIGURE 4: MARCH5 controls stress-induced degradation of MiD49. (A–H) Wild-type and MARCH5⁻/⁻ cells were treated with ActD (20 µM; A–D) or STS (1 µM; E–H), for 0, 2, 4, and 8 h, followed by Western blotting, as indicated. *, an x-reactive band detectable with anti-MARCH5 antibody; **, an x-reactive band likely resulting from STS-induced processing of an unrelated protein. In B–D and F–H, relative protein levels in cells treated as shown in A and E were quantified and plotted against the length of treatment with ActD (B–D) or STS (F–H). Data represent the mean ± SD of three independent experiments. Protein levels detected in untreated cells (time, 0 min) were set at 1. (I and J) Wild-type and MARCH5⁻/⁻ cells were treated with ActD or STS alone (lanes 5 and 10 in I and J) for 8 h or were cotreated with ActD and MG132 or STS and MG132 (lanes 1–4 and 6–9 in I and J, respectively) followed by Western blot. Tom20 was used as a loading control. *With this exposure, initial levels of Mcl1 in wild-type cells were barely detectable. (K–N) Wild-type and MARCH5⁻/⁻ cells were treated and analyzed as shown in A–H.

could contribute to the mitochondrial response to stress. These data also support the notion that not synthesis but degradation of MiD49 is altered by stress.

We also investigated MiD49 turnover in cells treated with agents directly affecting mitochondrial activity. To this end, wild-type and MARCH5⁻/⁻ cells were treated with an uncoupling agent, carbonyl cyanide 4-(trifluoromethoxy) phenylhydrazone (FCCP), and the OXPHOS complex III inhibitor AntA for 0, 2, 4, and 8 h and analyzed by Western blot (Figure 4, K–N, and Supplemental Figure S2A). As in the cases of ActD and STS treat-

ments, both FCCP (Figure 4, K–N), and to a lesser degree AntA (Supplemental Figure S2A), induced MARCH5-dependent reduction in MiD49. These data suggested that the specificity of MARCH5 for MiD49 could be controlled by the bioenergetic status of the mitochondria.

MARCH5 depletion sensitizes cells to stress-induced cell death

While MARCH5 depletion did not substantially affect mitochondrial fusion and bioenergetics under normal growth conditions (Figure 1),
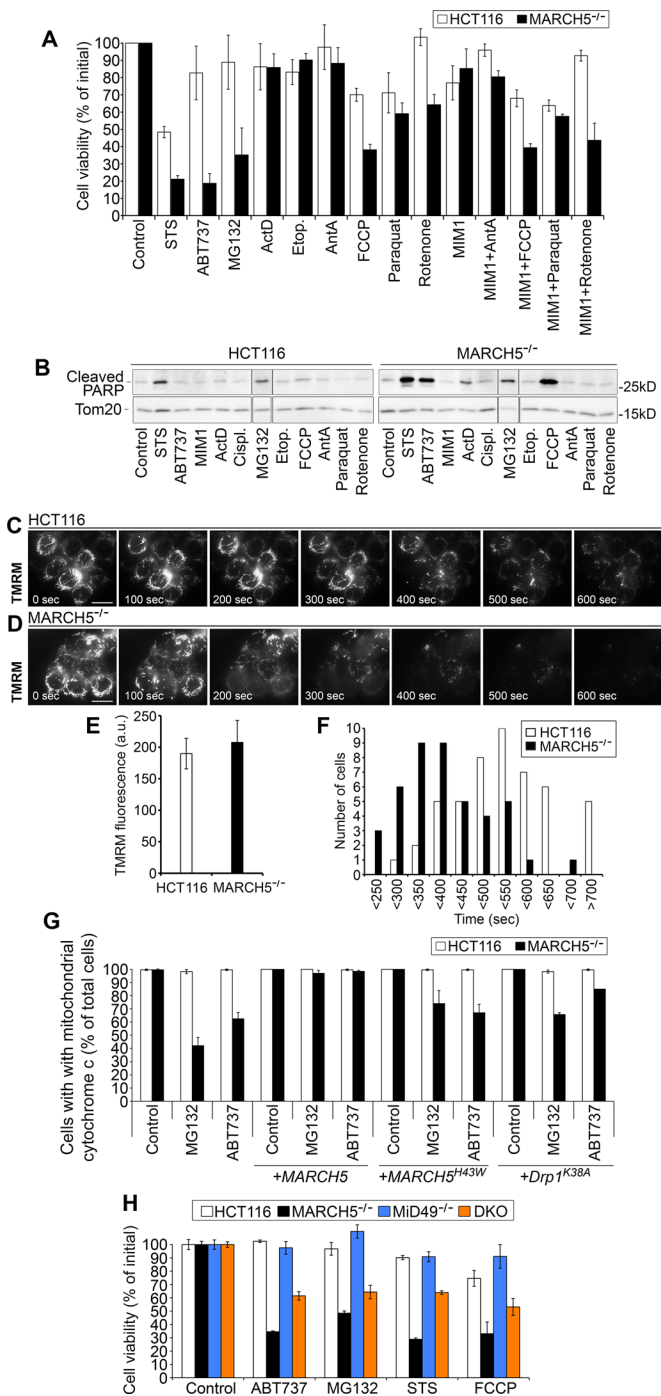
FIGURE 5: MARCH5 and stress-induced apoptosis. (A) Wild-type and MARCH5$^{-/-}$ cells were treated for 20 h with the compounds indicated in the figure, followed by cell viability assessment. Values obtained with untreated cells were set as 100%. Data represent mean ± SD of four measurements/condition from two to three experiments. (B) Total-cell lysates obtained from cells treated as indicated in the figure were analyzed by Western blot for cleavage of caspase substrate PARP. Cropped blots shown for specific treatments of wild-type and MARCH5$^{-/-}$ were from the same membranes. Tom20 was used as a loading control. (C–F) Wild-type (C) and MARCH5$^{-/-}$ (D) cells labeled with 100 nM TMRM were subjected to time-lapse imaging. In C and D, examples of images obtained at time points specified in the figure are shown. Scale bars: 20 µm. In E, initial TMRM fluorescence values obtained in the first frame images (0 s) in each time-lapse experiment were quantified. In F, the time needed for wild-type and MARCH5$^{-/-}$

cells to reach half of the initial TMRM fluorescence (TMRM $t_{1/2}$) was calculated. The number of cells reaching TMRM $t_{1/2}$ between specified imaging time frames is shown. Data in E and F represent 49 (wild-type) and 43 (MARCH5$^{-/-}$) time-lapse experiments, respectively. Data in E are shown as mean ± SD. (G) Cells were treated with the indicated compounds. In each group, cells retaining mitochondrial cytochrome c (nonapoptotic) and those showing cytosolic cytochrome c (apoptotic; for examples, see Supplemental Figure S2B) were counted. Data represent the mean ± SD of three independent counts of 150 cells/condition. (H) Wild-type, MARCH5$^{-/-}$, MiD49$^{-/-}$, and DKO (MARCH5$^{-/-}$/MiD49$^{-/-}$) cells were treated for 20 h with the compounds indicated in the figure, followed by cell viability assessment. Values obtained with untreated cells were set as 100%. Data represent mean ± SD of four measurements/condition.

the data (Figure 4) supported the possibility that MARCH5 could control mitochondrial response to stress. We analyzed the viability of wild-type and MARCH5$^{-/-}$ cells that were treated with an array of agents, including apoptosis inducers and mitochondrial toxins as indicated (Figure 5, A and B). The data showed significantly increased sensitivity of MARCH5$^{-/-}$ cells, as compared with wild-type cells, to cell death induced by several independent treatments (Figure 5A), suggesting a critical role for MARCH5 in mitochondrial and cellular stress responses.

Considering the high levels of Mcl1 in MARCH5$^{-/-}$ cells (Supplemental Figure S1, A and B), we also investigated the role of MARCH5 in Bcl2 family–regulated apoptotic cell death. To this end, we applied ABT737 and MIM1 compounds (Figure 5A and Supplemental Figure S2, B and C). While ABT737 selectively binds and inhibits Bcl2, Bcl-xL, and Bcl-w, it displays poor affinity for Mcl1 (Oltersdorf et al., 2005). MIM1 binds to and specifically inhibits Mcl1 (Cohen et al., 2012). The data showed that while MARCH5$^{-/-}$ cells were more sensitive to 2 µM ABT737-induced cell death, there was little or no effect with 10 µM MIM1 treatment, as compared with wild-type cells (Figure 5A). Considering the minor protective effects of higher MIM1 concentrations apparent in MARCH5$^{-/-}$ cells (Supplemental Figure S2C) and the fact that 10 µM MIM1 did not further increase MARCH5$^{-/-}$ cells' sensitivity to stress-induced apoptosis, it appears that Mcl1 accumulation is not sufficient to inhibit apoptosis in MARCH5-depleted cells. Western blot analysis of cleavage of the caspase substrate PARP (Figure 5B), a well-established apoptosis marker, confirmed the higher sensitivity of MARCH5$^{-/-}$ cells to stress-induced apoptosis. In addition, we applied imaging of the $\Delta\Psi_m$-sensitive fluorescent probe tetramethylrhodamine methyl ester (TMRM). TMRM can be used both to produce reactive oxygen species and mitochondrial damage and to monitor self-inflicted changes in $\Delta\Psi_m$ (Boyman et al., 2014). Wild-type (Figure 5C) and MARCH5$^{-/-}$ (Figure 5D) cells labeled with TMRM were subjected to time-lapse imaging with 10-s intervals and 10-ms exposure time set for all of experiments. Initial $\Delta\Psi_m$ (Figure 5E) and $\Delta\Psi_m$ changes over the time of imaging (Figure 5F) were quantified from several independent time-lapse experiments. While wild-type and MARCH5$^{-/-}$ cells showed similar initial values of $\Delta\Psi_m$ (Figure 5E), MARCH5$^{-/-}$ cells displayed higher sensitivity to TMRM imaging–induced mitochondrial depolarization, as compared with wild-type cells (Figure 5F). While wild-type cells displayed a 50% reduction in TMRM fluorescence (TMRM $t_{1/2}$) at ~500 s of imaging, the same reduction in TMRM occurred ~100 s earlier in MARCH5$^{-/-}$ cells (Figure 5F). Furthermore, MARCH5$^{-/-}$ cells showed higher sensitivity to OMM permeabilization, as assessed by cytochrome c translocation to the cytosol, compared with wild-type HCT116 cells (Figure 5G and

Supplemental Figure S2B). Cytochrome *c* release was completely inhibited by re-expression of MYC-MARCH5 (Figure 5G), while MYC-MARCH5^{H43W} showed a much lower inhibitory effect (Figure 5G). Supporting a role for mitochondrial fission in MARCH5$^{-/-}$ cells' sensitivity to apoptosis, expression of the dominant-negative Drp1 mutant (MYC-Drp1^{K38A}) also hindered cytochrome *c* release, albeit to a lesser degree than MYC-MARCH5 (Figure 5G). We also tested the effect of MiD49 depletion in MARCH5$^{-/-}$ cell sensitivity to stress-induced apoptosis (Figure 5H). Cells were treated with ABT737, MG123, STS, and FCCP, compounds that strongly affect MARCH5$^{-/-}$ cell survival (Figure 5A), and were analyzed for cell viability. The data showed a notable reduction of DKO cells' sensitivity to apoptosis induced by the above-mentioned compounds, as compared with MARCH5$^{-/-}$ cells (Figure 5H). Thus abnormal accumulation of MiD49 in MARCH5$^{-/-}$ cells is likely to contribute to sensitivity of MARCH5$^{-/-}$ cells to stress-induced apoptosis. However, because DKO cells were less viable than wild-type cells (Figure 5H), it is likely that MARCH5 controls apoptosis in both MiD49 regulation–dependent, and MiD49 regulation–independent manners. Thus investigation into other apoptosis-related factors controlled by MARCH5 is needed.

In summary, the data support a critical role for MARCH5 in the regulation of mitochondrial fission and cell viability. Through ubiquitin- and proteasome-dependent degradation of MiD49, MARCH5 acts as a negative regulator of mitochondrial fission and thereby initiates a mechanism that affords the cell protection from stress-induced apoptosis.

MATERIALS AND METHODS

Cell culture and transfection
HCT116 cells were cultured in McCoy's 5a (modified) medium supplemented with 10% heat-inactivated fetal bovine serum (FBS), 1 mM sodium pyruvate, MEM nonessential amino acids (Gibco, Waltham MA), 100 U/ml penicillin, and 100 mg/ml streptomycin in 5% CO_2 at 37°C. Other cells were grown in DMEM with the same supplements and under the same growth conditions as above. Cells were transfected with either X-treme GENE HP DNA transfection reagent (Roche, Basel, Switzerland; most of the imaging studies) or Lipofectamine 2000 (LifeTechnologies, Carlsbad, CA; protein biochemistry studies), according to the manufacturers' instructions. The fine-tuned transfection conditions resulted in >50% of cells being transfected using Lipofectamine 2000. Cells were used for analyses at 14–20 h after transfection.

Generation of MARCH5$^{-/-}$ cells
To make a gene-targeting construct (KO), two 1-kb sequences flanking targeted exon 2 of the human *MARCH5* gene were amplified from HCT116 genomic DNA and ligated with pAAV-MCS (Stratagene, San Diego, CA), and the Neo cassette was cut out from the pSEPT vector (a gift from Fred Bunz, Johns Hopkins University), as previously described (Topaloglu *et al.*, 2005). The pAAV-MARCH5 plasmid was cotransfected with pAAV-RC and pHelper into AAV-293 cells for virus packaging. HCT116 cells were infected with the pAAV-RC virus and selected with G418. To obtain a biallelic MARCH5 knockout (MARCH$^{-/-}$), we used heterozygous MARCH5$^{+/-}$cells for a second round of gene targeting with the protocol described above.

CRISP/Cas9 generation of MiD49$^{-/-}$ cells
The specific targeted sites of CRISP/Cas9 were researched using the ChopChop Web tool (https://chopchop.rc.fas.harvard.edu; Montague *et al.*, 2014), and two pairs of guide RNA (gRNA) target sites with the highest scores were picked out. The first pair of gRNAs were RNA1 (gRNA1): 5'-GCAGAGTTCTCCCAGAAACGGGG-3';

and gRNA2: 5'-GGCCACTAGCCCGCGGGATGAGG-3'. The second pair of gRNAs were gRNA1: 5'-GCAGAGTTCTCCCAGAAAC-GGGG-3'; and gRNA3: 5'-TGTGTCTGACACTGCAGGAGAGG-3'. gRNA sequences were cloned by PCR with the following primers: F1: 5'-TTTCTTGGCTTTATATATCTTGTGGAAAGGACGAAACACCG CAGAGTTCTCCCAGAAACG-3'; R1: 5'-GACTAGCCTTATTTTAAC-TTGCTATTTCTAGCTCTAAAACCGTTTCTGGGAGAACTCTGC-3'; F2: 5'-TTTCTTGGCTTTATATATCTTGTGGAAAGGACGAAACACCG GCCACTAGCCCGCGGGATG-3'; R2: 5'-GACTAGCCTTATTTTAAC TTGCTATTTCTAGCTCTAAAACCATCCCGCGGGCTAGTGGCC-3'; F3: 5'-TTTCTTGGCTTTATATATCTTGTGGAAAGGACGAAACACC-GGTGTCTGACACTGCAGGAG-3'; R3: 5'-GACTAGCCTTATTTTA-ACTTGCTATTTCTAGCTCTAAAACCTCCTGCAGTGTCAGA-CACC-3'. The PCR products were incorporated into *Afl*II-linearized gRNA cloning vector (www.addgene.org/41824) using Gibson assembly, as previously described (Mali *et al.*, 2013). The resulting plasmids were verified by sequence analysis. Each pair of gRNA plasmids was cotransfected with Cas9 into HCT116 wild-type cells and MARCH5$^{-/-}$ HCT116 cells. Single-cell MiD49$^{-/-}$ clones with biallelic MiD49 knockout were identified with PCR and Western blot.

Expression constructs and shRNA
MYC-MARCH5, YFP-MARCH5, and YFP-MARCH5^{H43W} were generated and described earlier (Karbowski *et al.*, 2007). pcDNA3.1(-) MiD49 4×MYC His×6 (Loson *et al.*, 2013) was a gift from David Chan (California Institute of Technology, Pasadena, CA; Addgene plasmid #4459). PCR amplifications were performed using 5'-CTGCAG-GAATTCGATATGCCGGACCAAGCCCTACAG-3' as the forward primer and 5'-ATCGATAAGCTTGATTTACTGTTTGAAGTAAACTT-TAAATG-3' as the backward primer with MYC-MARCH5 and YFP-MARCH5^{H43W} as templates, respectively. The resulting products were then cloned into *Eco*RV-linearized pCMV-3Tag-7 mammalian expression vector (Agilent Technologies, Santa Clara, CA) using Gibson assembly to generate the MYC-tagged MARCH5-truncated mutants, M5ΔC and M5H43W/ΔC. All RNAi experiments were performed using MISSION shRNA vectors purchased from Sigma-Aldrich (St. Louis, MO). p97 RNAis (RNAi 1 [Sigma plasmid #TRCN0000004250] and RNAi 2 [Sigma plasmid #TRCN0000004252]) were described previously (Xu *et al.*, 2011). MARCH5 (RNAi 1 [Sigma plasmid #TRCN0000037014], RNAi 2 [Sigma plasmid #TRCN0000037015], RNAi 3 [Sigma plasmid #TRCN0000037016], RNAi 4 [Sigma plasmid #TRCN00000370170], and RNAi 5 [Sigma plasmid #TRCN0000037018]), was down-regulated with the above-mentioned shRNA vectors. An eGFP-targeting shRNA construct was used as a control (Sigma plasmid #SHC005; Xu *et al.*, 2011). Cells were transfected with respective shRNA constructs and at ~24 h posttransfection were incubated with 3 μg/ml puromycin for an additional 4–5 d to select transfected cells.

Immunofluorescence
Immunofluorescence labeling was performed as previously described (Benard *et al.*, 2010; Li *et al.*, 2015). Briefly, cells grown in 2-well chamber slides (model 1 German borosilicate; Labtec, Waltham, MA) were fixed with prewarmed 37°C 4% paraformaldehyde in phosphate-buffered saline (PBS) solution for 20 min at room temperature (RT), then permeabilized with 0.15% Triton X-100 in PBS for 20 min at RT. After being blocked with 7.5% bovine serum albumin (BSA) in PBS for 45 min, samples were incubated with primary antibodies in 7.5% BSA in PBS for 90 min at RT; this was followed by three washes with 7.5% BSA in PBS and incubation with secondary antibodies diluted in blocking buffer for 45 min at RT. Samples were washed with PBS at RT and imaged directly in PBS

within 2 d after immunofluorescence processing. The primary antibodies were: anti-Tom20 polyclonal antibody (Santa Cruz, Dallas, TX), anti-MiD49 polyclonal antibody (ProteinTech, Tucson, AZ), anti-Mcl1 monoclonal antibody (mAb; Santa Cruz), anti-Drp1 mAb (BD Biosciences, Franklin Lakes, NJ), anti cytochrome *c* mAb (BD Biosciences), anti-hemagglutinin tag mAb (Abcam, Cambridge, UK), anti-MYC tag mAb (Roche), and anti-MYC tag polyclonal antibody (provided by Mervyn Monteiro, University of Maryland School of Medicine). Secondary antibodies were anti-mouse or anti-rabbit Alexa Fluor 488 (Life Technologies), anti-mouse or anti-rabbit Alexa Fluor 546 (Life Technologies), and anti-rabbit Alexa Fluor 637 (Life Technologies).

Image acquisition and analysis

Images were acquired with a Zeiss LSM 880 confocal microscope equipped with Airyscan superresolution imaging module, using a 63×/1.40 NA Plan-Apochromat Oil DIC M27 objective lens (Zeiss MicroImaging, Jena, Germany). Z-stacks covering the whole depth of cells with the interval of 0.018 µm were acquired, followed by Airyscan image processing (set at 7) and analyses using ZEN image acquisition and processing software (Zeiss MicroImaging). Maximum intensity projections shown in the figures were also obtained using ZEN software. Image cropping and global adjustments to brightness and contrast were performed using Adobe Photoshop CS6 software (Adobe Systems, San Jose, CA). Live-cell imaging was performed using Zeiss Axio Observer Z1 fluorescence microscope equipped with a 100×/1.45 NA a-Plan-FLUAR objective lens (Zeiss MicroImaging), an ApoTome unit (enabling high-resolution, structured-illumination image acquisition), a Definitive Focus module, and a charge-coupled device camera (QuantEM 512SC; Photometrics) at RT, as previously described (Benard *et al.*, 2010; Xu *et al.*, 2011; Li *et al.*, 2015). The software used for image acquisition was AxioVision 4.8 (Zeiss MicroImaging). Cells were grown in two-well chamber slides (model 1 German borosilicate; Labtec) and imaged in Phenol Red–free DMEM, supplemented with 10% heat-inactivated FBS, 2 mM Glutamax, 1 mM sodium pyruvate, MEM nonessential amino acids, 100 U/ml penicillin, and 100 mg/ml streptomycin and 25 mM HEPES (pH 7.4) at RT.

Cell lysates, Western blot, and immunoprecipitation

Cells were harvested, and total-cell protein lysates and subcellular fractions were prepared as previously described (Benard *et al.*, 2010; Xu *et al.*, 2011; Li *et al.*, 2015). For total-cell lysates, cells were collected, washed with ice-cold PBS, suspended in SDS–PAGE sample buffer, and incubated at 100°C for 10 min. Mitochondria-enriched heavy membrane fractions were generated as previously described (Benard *et al.*, 2010; Xu *et al.*, 2011). Briefly, cells were washed once with ice-cold PBS and scraped into 15-ml tubes in ice-cold PBS; this was followed by centrifugation at 500 × *g* for 5 min. The cell pellets were resuspended in ~3 volumes of fractionation buffer (10 mM HEPES, 10 mM NaCl, 1.5 mM MgCl$_2$, protease inhibitors [Roche]). Cells were then passed 12 times through a 25-G needle attached to a 1-ml syringe to disrupt cell membranes. This suspension was centrifuged at 2500 × *g* at 4°C for 5 min to remove unbroken cells and cell debris. The supernatant was centrifuged at 6000 × *g* at 4°C for 10 min to pellet the heavy membrane (HM) fraction. The supernatants were used as postmitochondrial cytosolic fractions. For reduction of cytosolic contamination, the HM fractions were washed in ice-cold PBS and recentrifuged at 8000 × *g*. Protein concentrations were measured directly in the samples using a Nano-Drop 1000 spectrophotometer (Thermo Scientific, Waltham, MA). Proteins were separated on 4–20% gradient Tris-glycine polyacryl-amide gels (Invitrogen, Carlsbad, CA), transferred onto polyvinylidene fluoride membranes (Immobilon-P; Millipore, Billerica, MA), and incubated with primary antibodies followed by horseradish peroxidase–conjugated anti-mouse (Roche) or anti-rabbit (Roche) secondary antibodies. Blots were detected with Super Signal West Pico ECL reagent (Thermo Scientific Biosciences) using an ImageQuant LAS4000 chemiluminescence imager (GE Healthcare Life Sciences, Marlborough, MA). Antibodies used for Western blotting were: anti-MARCH5 polyclonal antibody (Millipore), anti-MiD49 polyclonal antibody (Sigma), anti-MiD51 polyclonal antibody (ProteinTech), anti-Mff polyclonal antibody (ProteinTech), anti-Drp1 mAb (Dlp1; BD Biosciences), anti-Fis1 polyclonal antibody (Abcam), anti-endophilin B1 mAb (Bif1; Imgenex), anti-p97 polyclonal antibody (Cell Signaling, Danvers, MA), anti-Mcl1 mAb (Santa Cruz), anti-Tom20 polyclonal antibody (Santa Cruz), anti-Tom22 polyclonal antibody (ProteinTech), anti-Tom40 polyclonal antibody (Santa Cruz), anti-Tom70 polyclonal antibody (ProteinTech), anti-Tim23 mAb (BD Biosciences), anti-Complex II-70 kDa mAb (Mitosciences); anti-OXPHOS human WB antibody cocktail (Abcam); anti-MYC tag mAb (Roche), anti-Bcl2 mAb (BD Biosciences), anti-Bcl-xL mAb (Cell Signaling), anti-Bak polyclonal antibody (Upstate), anti-Bax polyclonal antibody (Santa Cruz), anti-Bid mAb (BD Biosciences), anti-PUMA polyclonal antibody (Abcam), anti-VDAC1 polyclonal antibody (Cell Signaling), anti-Opa1 mAb (BD Biosciences), anti-Mfn2 mAb (Abcam), anti-Ub mAb (Santa Cruz), anti-K48 Ub mAb (Millipore), anti p62 mAb (BD Biosciences), anti-LC3A mAb (Cell Signaling), anti-GAPDH mAb (BD Biosciences), and anti-PARP mAb (Abcam). Immunoprecipitation under denaturing conditions was performed as previously described (Tanaka *et al.*, 2010; Xu *et al.*, 2011). Briefly, cells were collected and suspended in denaturing buffer (1% SDS, 5 mM EDTA, 10 mM β-mercaptoethanol). Samples were incubated at 100°C for 10 min, centrifuged to remove unsolubilized material, and diluted 10 times with ice-cold IP buffer (20 mM Tris-HCl, pH 7.5, 150 mM NaCl, 1 mM EDTA, 0.5% NP-40, 5 mM N-ethylmaleimide, and protease inhibitors). Proteins were immunoprecipitated using either MYC-tagged agarose beads or incubation with anti-Mcl1 mAb (Santa Cruz), followed by protein A/G agarose beads. For quantification of protein levels, intensities of specific proteins were analyzed using ImageJ software (National Institutes of Health, Bethesda, MD).

Mitochondrial fusion assay

A mito-PAGFP–based mitochondrial fusion assay (Karbowski *et al.*, 2004, 2014) was performed using a Zeiss LSM 510 META confocal microscope (Zeiss MicroImaging) equipped with Plan-Apochromat 100×/ 1.4 NA oil DIC M27 objective lens (Zeiss MicroImaging) as previously described (Li *et al.*, 2015). Briefly, after acquisition of a preactivation image, a ~5-µm-diameter circular region of interest was photoactivated by brief irradiation with 351/364-nm light (Coherent Enterprise Ion Laser 80.0 mW); this was followed by time-lapse imaging using a 488-nm excitation light (488-nm Argon Ion Laser 25.0 mW set at 0.3%). Fifteen postactivation images were collected, with the interval between images set to ~2 min. To avoid *z*-section shift, focus was maintained using "Multi-time Macro" and the autofocusing system (which utilizes line scans to detect the reflection off the coverglass). Images were acquired and analyzed using ZEN 2009 image acquisition software (Zeiss MicroImaging). For quantification of the dynamics of mitochondrial fusion, the time-lapse images of each cell were analyzed using ImageJ software. Briefly, after setting a threshold, 17 time-lapse images of each single-cell time-lapse experiment were converted to binary images using the brightest pixels from the first image (preactivated). Pixels in the consecutive 16 images (postactivation images) that exceeded

this fluorescence intensity threshold were taken as containing activated mito-PAGFP signal and were assigned a value of 1; other pixels were taken as background and assigned with a value of 0. The pixels with mito-PAGFP signal were summed as a measure of the cellular area with activated mito-PAGFP. The time-dependent mito-PAGFP–containing area obtained for each cell was normalized with respect to its maximal and minimal values. The results from multiple cells were aligned with respect to the time at which each cell reached the maximally activated area. The time-dependent results were averaged together.

Bioenergetics

Cellular oxygen consumption was measured using the Seahorse XF24 Extracellular Flux Analyzer at 24 h postplating of 3×10^4 cells/well, as previously described (Clerc et al., 2012). Experiments were performed in XF24 medium consisting of 120 mM NaCl, 3.5 mM KCl, 1.3 mM $CaCl_2$, 0.4 mM KH_2PO_4, 1 mM $MgCl_2$, 4 mg/ml fatty acid–free BSA, 5 mM 4-(2-hydroxyethyl)-1-piperazineethanesulfonic acid (HEPES), and 15 mM glucose (pH 7.4) at 37°C (Clerc et al., 2012). Drug treatments were titrated and optimized for each cell type; they included 0.2–0.5 µg/ml oligomycin, 1–2 µM FCCP, and 1 µM AntA. Pyruvate (10 mM) was included with the addition of FCCP to ensure endogenous substrate supply was not rate limiting during the measurement of maximal respiration.

Cell viability assay

HCT116 cells were seeded in 96-well opaque plates (3×10^4 cells/well) and incubated with vehicle (0.2% dimethyl sulfoxide), STS (0.2 µM), actinomycin D (20 µM), ABT737 (2 µM), etoposide (10 µM), FCCP (50 µM), AntA (50 µM), paraquat (2 mM), rotenone (50 µM), MIM1 (1 µM, 10 µM, 25 µM, and 100 µM), and MG132 (10 µM), alone or in combination. Cell viability was analyzed at 20 h using the CellTiter-Glo Luminescent Cell Viability Assay, according to the manufacturer's protocol (Promega, Madison, WI). Luminescence was measured using a Clario Star plate reader (BMG Labtech, Ortenberg, Germany). Values obtained in control cells were normalized to 100% viability.

REFERENCES

Benard G, Neutzner A, Peng G, Wang C, Livak F, Youle RJ, Karbowski M (2010). IBRDC2, an IBR-type E3 ubiquitin ligase, is a regulatory factor for Bax and apoptosis activation. EMBO J 29, 1458–1471.

Boyman L, Chikando AC, Williams GS, Khairallah RJ, Kettlewell S, Ward CW, Smith GL, Kao JP, Lederer WJ (2014). Calcium movement in cardiac mitochondria. Biophys J 107, 1289–1301.

Chan DC (2012). Fusion and fission: interlinked processes critical for mitochondrial health. Annu Rev Genet 46, 265–287.

Clerc P, Carey GB, Mehrabian Z, Wei M, Hwang H, Girnun GD, Chen H, Martin SS, Polster BM (2012). Rapid detection of an ABT-737-sensitive primed for death state in cells using microplate-based respirometry. PLoS One 7, e42487.

Cohen NA, Stewart ML, Gavathiotis E, Tepper JL, Bruekner SR, Koss B, Opferman JT, Walensky LD (2012). A competitive stapled peptide screen identifies a selective small molecule that overcomes MCL-1-dependent leukemia cell survival. Chem Biol 19, 1175–1186.

Fang L, Li J, Flammer J, Neutzner A (2013). MARCH5 inactivation supports mitochondrial function during neurodegenerative stress. Front Cell Neurosci 7, 176.

Gandre-Babbe S, van der Bliek AM (2008). The novel tail-anchored membrane protein Mff controls mitochondrial and peroxisomal fission in mammalian cells. Mol Biol Cell 19, 2402–2412.

Germain M, Nguyen AP, Le Grand JN, Arbour N, Vanderluit JL, Park DS, Opferman JT, Slack RS (2011). MCL-1 is a stress sensor that regulates autophagy in a developmentally regulated manner. EMBO J 30, 395–407.

Hailey DW, Rambold AS, Satpute-Krishnan P, Mitra K, Sougrat R, Kim PK, Lippincott-Schwartz J (2010). Mitochondria supply membranes for autophagosome biogenesis during starvation. Cell 141, 656–667.

Inuzuka H, Shaik S, Onoyama I, Gao D, Tseng A, Maser RS, Zhai B, Wan L, Gutierrez A, Lau AW, et al. (2011). SCF(FBW7) regulates cellular apoptosis by targeting MCL1 for ubiquitylation and destruction. Nature 471, 104–109.

Karbowski M (2010). Mitochondria on guard: role of mitochondrial fusion and fission in the regulation of apoptosis. Adv Exp Med Biol 687, 131–142.

Karbowski M, Arnoult D, Chen H, Chan DC, Smith CL, Youle RJ (2004). Quantitation of mitochondrial dynamics by photolabeling of individual organelles shows that mitochondrial fusion is blocked during the Bax activation phase of apoptosis. J Cell Biol 164, 493–499.

Karbowski M, Cleland MM, Roelofs BA (2014). Photoactivatable green fluorescent protein-based visualization and quantification of mitochondrial fusion and mitochondrial network complexity in living cells. Methods Enzymol 547, 57–73.

Karbowski M, Neutzner A, Youle RJ (2007). The mitochondrial E3 ubiquitin ligase MARCH5 is required for Drp1 dependent mitochondrial division. J Cell Biol 178, 71–84.

Li S, Xu S, Roelofs BA, Boyman L, Lederer WJ, Sesaki H, Karbowski M (2015). Transient assembly of F-actin on the outer mitochondrial membrane contributes to mitochondrial fission. J Cell Biol 208, 109–123.

Liu T, Yu R, Jin SB, Han L, Lendahl U, Zhao J, Nister M (2013). The mitochondrial elongation factors MIEF1 and MIEF2 exert partially distinct functions in mitochondrial dynamics. Exp Cell Res 319, 2893–2904.

Loson OC, Song Z, Chen H, Chan DC (2013). Fis1, Mff, MiD49, and MiD51 mediate Drp1 recruitment in mitochondrial fission. Mol Biol Cell 24, 659–667.

Mali P, Yang L, Esvelt KM, Aach J, Guell M, DiCarlo JE, Norville JE, Church GM (2013). RNA-guided human genome engineering via Cas9. Science 339, 823–826.

Mishra P, Chan DC (2014). Mitochondrial dynamics and inheritance during cell division, development and disease. Nat Rev Mol Cell Biol 15, 634–646.

Montague TG, Cruz JM, Gagnon JA, Church GM, Valen E (2014). CHOPCHOP: a CRISPR/Cas9 and TALEN web tool for genome editing. Nucleic Acids Res 42, W401–W407.

Nakamura N, Hirose S (2008). Regulation of mitochondrial morphology by USP30, a deubiquitinating enzyme present in the mitochondrial outer membrane. Mol Biol Cell 19, 1903–1911.

Nakamura N, Kimura Y, Tokuda M, Honda S, Hirose S (2006). MARCH-V is a novel mitofusin 2- and Drp1-binding protein able to change mitochondrial morphology. EMBO Rep 7, 1019–1022.

Narendra D, Tanaka A, Suen DF, Youle RJ (2008). Parkin is recruited selectively to impaired mitochondria and promotes their autophagy. J Cell Biol 183, 795–803.

Oltersdorf T, Elmore SW, Shoemaker AR, Armstrong RC, Augeri DJ, Belli BA, Bruncko M, Deckwerth TL, Dinges J, Hajduk PJ, et al. (2005). An inhibitor of Bcl-2 family proteins induces regression of solid tumours. Nature 435, 677–681.

Palmer CS, Elgass KD, Parton RG, Osellame LD, Stojanovski D, Ryan MT (2013). Adaptor proteins MiD49 and MiD51 can act independently of Mff and Fis1 in Drp1 recruitment and are specific for mitochondrial fission. J Biol Chem 288, 27584–27593.

Palmer CS, Osellame LD, Laine D, Koutsopoulos OS, Frazier AE, Ryan MT (2011). MiD49 and MiD51, new components of the mitochondrial fission machinery. EMBO Rep 12, 565–573.

Park YY, Lee S, Karbowski M, Neutzner A, Youle RJ, Cho H (2010). Loss of MARCH5 mitochondrial E3 ubiquitin ligase induces cellular senescence through dynamin-related protein 1 and mitofusin 1. J Cell Sci 123, 619–626.

Schwickart M, Huang X, Lill JR, Liu J, Ferrando R, French DM, Maecker H, O'Rourke K, Bazan F, Eastham-Anderson J, *et al.* (2010). Deubiquitinase USP9X stabilizes MCL1 and promotes tumour cell survival. Nature 463, 103–107.

Sugiura A, Nagashima S, Tokuyama T, Amo T, Matsuki Y, Ishido S, Kudo Y, McBride HM, Fukuda T, Matsushita N, *et al.* (2013). MITOL regulates endoplasmic reticulum-mitochondria contacts via Mitofusin2. Mol Cell 51, 20–34.

Sugiura A, Yonashiro R, Fukuda T, Matsushita N, Nagashima S, Inatome R, Yanagi S (2011). A mitochondrial ubiquitin ligase MITOL controls cell toxicity of polyglutamine-expanded protein. Mitochondrion 11, 139–146.

Tanaka A, Cleland MM, Xu S, Narendra DP, Suen DF, Karbowski M, Youle RJ (2010). Proteasome and p97 mediate mitophagy and degradation of mitofusins induced by Parkin. J Cell Biol 191, 1367–1380.

Topaloglu O, Hurley PJ, Yildirim O, Civin CI, Bunz F (2005). Improved methods for the generation of human gene knockout and knockin cell lines. Nucleic Acids Res 33, e158.

Xu S, Peng G, Wang Y, Fang S, Karbowski M (2011). The AAA-ATPase p97 is essential for outer mitochondrial membrane protein turnover. Mol Biol Cell 22, 291–300.

Yonashiro R, Ishido S, Kyo S, Fukuda T, Goto E, Matsuki Y, Ohmura-Hoshino M, Sada K, Hotta H, Yamamura H, *et al.* (2006). A novel mitochondrial ubiquitin ligase plays a critical role in mitochondrial dynamics. EMBO J 25, 3618–3626.

Yonashiro R, Sugiura A, Miyachi M, Fukuda T, Matsushita N, Inatome R, Ogata Y, Suzuki T, Dohmae N, Yanagi S (2009). Mitochondrial ubiquitin ligase MITOL ubiquitinates mutant SOD1 and attenuates mutant SOD1-induced reactive oxygen species generation. Mol Biol Cell 20, 4524–4530.

Youle RJ, Strasser A (2008). The BCL-2 protein family: opposing activities that mediate cell death. Nat Rev Mol Cell Biol 9, 47–59.

Youle RJ, van der Bliek AM (2012). Mitochondrial fission, fusion, and stress. Science 337, 1062–1065.

Zhong Q, Gao W, Du F, Wang X (2005). Mule/ARF-BP1, a BH3-only E3 ubiquitin ligase, catalyzes the polyubiquitination of Mcl-1 and regulates apoptosis. Cell 121, 1085–1095.